Modeling of MoS_2-based Nanotransistor

Difan Wen, Elias Lehman, Nikolai Semenov

December 15, 2023

Abstract

In this project, we performed electronic bandstructure calculations of monolayer MoS_2 using Slater–Koster tight-binding approximation and applied quasi-ballistic transport model to obtain an analytical drain current expression for MoS_2-based transistor. Finally, we compared our results to existing data in the literature to both validate our model.

1 Introduction

The pursuit of the semiconductor industry continues to drive transistors to nanoscale dimensions while maintaining high power efficiency. As transistors continue to scale down, conventional silicon-based field-effect transistors (FETs) suffer from short-channel effects, adversely affecting their performance and reliability. Two-dimensional (2D) materials, such as transition metal dichalcogenides (TMDs) and graphene, emerge as promising alternatives due to their exceptional electrical properties. These materials have the potential to overcome the limitations of traditional silicon FETs, offering improved performance and scalability at nanoscale dimensions. Among these materials, TMDs and graphene heterostructures are particularly important for their electrical characteristics, which make them suitable for transistor applications. In this context, we perform modeling of a monolayer MoS_2 transistor with graphene as metal contacts. Our focus is on analyzing the current-voltage (IV) characteristics from the experimental results in [1] using the using Slater–Koster tight-binding approximation and applied quasi-ballistic transport model to obtain an analytical drain current expression.

2 Bandstrucure Calculation

The structure of monolayer MoS_2 is shown in Fig. 1a) with lattice vectors $a_1 = a(1,0), a_2 = a(-1/2, \sqrt{3}/2)$ and reciprocal-space vectors $b_1 = \frac{2\pi}{a}(1, 1/\sqrt{3})$ and $b_2 = \frac{4\pi}{a\sqrt{3}}(0,1)$. The lattice constant of MoS_2 is $3.16\mathring{A}$. The Brilouin zone is show in Fig. 1c) with the high-symmetry points $\Gamma = (0,0), K = 4\pi/3a(1,0)$ and $M = 4\pi/3a(0, \sqrt{3}/2)$. The electronic bandstructure of MoS_2 was analyzed through Slater–Koster tight-binding (TB) formalism presented in [2]. Under this formalism, the relevant atomic orbital basis for a monolayer is the orbitals of each atom, labeled as

$$\hat{\psi}^\dagger_{pd} = \left[\hat{d}^\dagger_{z^2}, \hat{d}^\dagger_{xy}, \hat{d}^\dagger_{x^2-y^2}, \hat{d}^\dagger_{xz}, \hat{d}^\dagger_{yz},\ \hat{p}^{A\dagger}_x, \hat{p}^{A\dagger}_y, \hat{p}^{A\dagger}_z, \hat{p}^{B\dagger}_x, \hat{p}^{B\dagger}_y, \hat{p}^{B\dagger}_z\right].$$

Due to the symmetry present in the structure, the orbital is mapped to a new basis Table. 5,

$$\hat{\phi}^\dagger_{\text{eo}} = \left[\hat{d}^{(\text{o})\dagger}_{xz}, \hat{d}^{(\text{o})\dagger}_{yz}, \hat{p}^{(\text{o})\dagger}_z, \hat{p}^{(\text{o})\dagger}_x, \hat{p}^{(\text{o})\dagger}_y,\ \hat{d}^{(\text{e})\dagger}_{z^2}, \hat{d}^{(\text{e})\dagger}_{xy}, \hat{d}^{(\text{e})\dagger}_{x^2-y^2}, \hat{p}^{(\text{e})\dagger}_z, \hat{p}^{(\text{e})\dagger}_x, \hat{p}^{(\text{e})\dagger}_y\right]$$

The hopping terms are visualized in Fig. 1b) with hopping vectors given in Table 1. The connected orbitals in the different hopping terms of the Hamiltonian are defined in the Appendix.

The expressions and fitting parameters for the TB model are given in Appendix and [2]. The bandstructure calculated from this model is plotted in Fig.2a) and compared to electronic bandstructure from DFT calculations in Fig.2b) [3]. The effective masses at the **K** point are determined to be $m^*_e = 0.505m_0$ for electrons and $m^*_h = 0.448m_0$ for holes after quadratic fitting using $\hbar^2/\frac{\partial^2 E}{\partial k^2}$, which is comparable to the result presented in [4]. The ballistic injection velocity is given by $v_T\left(\frac{1-e^{-\frac{eV_{DS}}{k_BT}}}{1+e^{-\frac{eV_{DS}}{k_BT}}}\right)$, where $v_T = \sqrt{2k_BT/\pi m^*} \approx 7.6 \times 10^6$ cm/s. The group velocity is calculated from the band structure near the **K** point is shown in Fig. 2 c) and d), where $v = \frac{\partial \omega}{\partial k} = \frac{1}{\hbar}\frac{\partial E}{\partial k} \approx \times 10^7$ cm/s.

$t^{(1)}, t^{(2)}, t^{(3)}$	$\boldsymbol{\delta}_1 = \boldsymbol{a}_1, \boldsymbol{\delta}_2 = \boldsymbol{a}_1 + \boldsymbol{a}_2, \boldsymbol{\delta}_3 = \boldsymbol{a}_2$
$t^{(4)}, t^{(5)}$	$\boldsymbol{\delta}_4 = -\left(2\boldsymbol{a}_1 + \boldsymbol{a}_2\right)/3, \boldsymbol{\delta}_5 = \left(\boldsymbol{a}_1 + 2\boldsymbol{a}_2\right)/3$ $\boldsymbol{\delta}_6 = \left(\boldsymbol{a}_1 - \boldsymbol{a}_2\right)/3$
$t^{(6)}$	$\boldsymbol{\delta}_7 = -2\left(\boldsymbol{a}_1 + 2\boldsymbol{a}_2\right)/3, \boldsymbol{\delta}_8 = 2\left(2\boldsymbol{a}_1 + \boldsymbol{a}_2\right)/3$ $\boldsymbol{\delta}_9 = 2\left(\boldsymbol{a}_2 - \boldsymbol{a}_1\right)/3$

Table 1: Hopping vectors

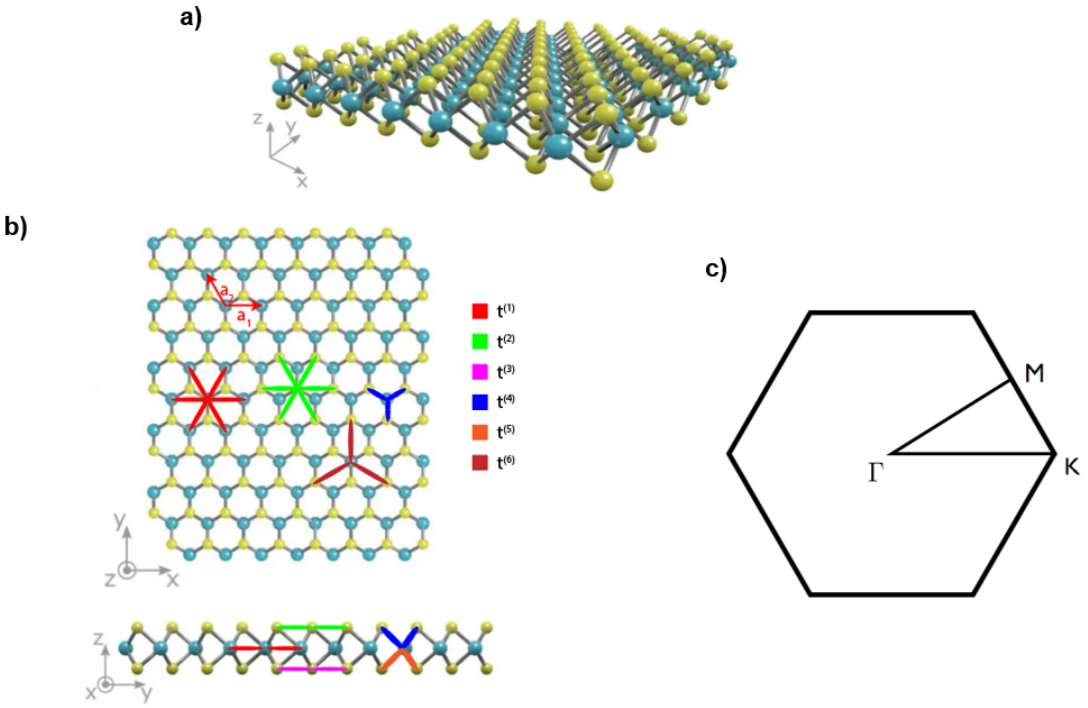

Figure 1: a) Atomic structure of monolayer MoS_2 b) The crystal structure of monolayer MoS_2 with all hopping terms in the tight-binding formalism: Mo-Mo coupling with first-neighbor pairs ($t^{(1)}$); S-S coupling with first-neighbor pairs ($t^{(2)}, t^{(3)}$); S-Mo coupling of with neighbor pairs ($t^{(4)}, t^{(5)}, t^{(6)}$). c) Brillouin zone of monolayer MoS_2.

3 Data Extraction from Literature

To extract data from the analyzed publication [1] we use an online plot digitizer.

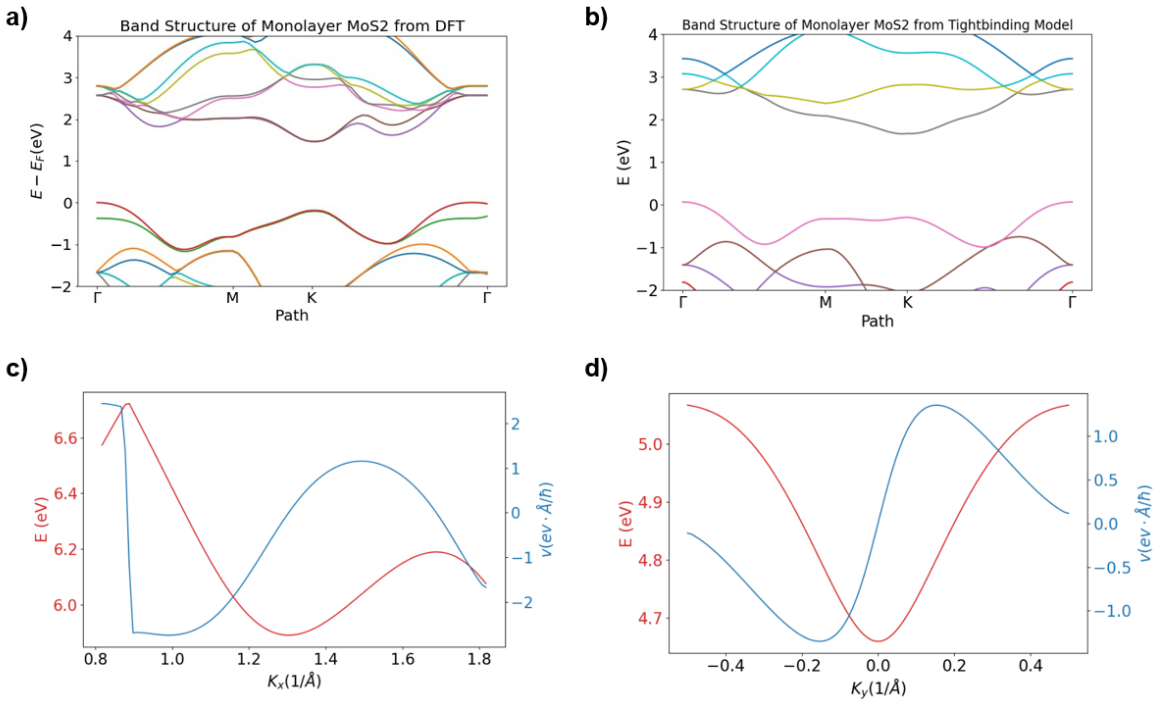

Figure 2: a) Bandstructure of monolayer MoS_2 from DFT. b) Bandstructure of monolayer MoS_2 from tight-binding model. c) The group velocity near the K-point in the x. d) The group velocity near the K-point in the y direction.

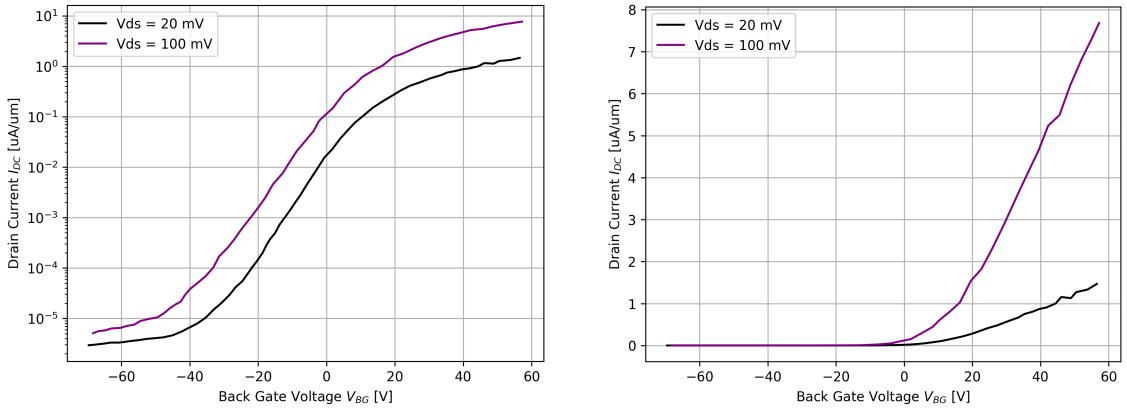

(a) (b)

Figure 3: Example of data extraction. (a) Digitized Figure 3c from [1]; (b) same figure in linear scale for clarity.

4 Modeling MOSFET

4.1 Primary Model: Numeric Quasi-Ballistic

4.1.1 Description

To investigate the dependence of drain current on drain voltage, we utilize the following model, which is highly inspired by the numerical quasi-ballistic approach found in [5]. The drain-source current can be expressed using positive- and negative-going fluxes:

$$I_{\mathrm{DS}} = 2Wq\left[F^{+}(0) - F^{-}(0)\right], \tag{1}$$

where q is the elementary charge, W is the channel width, and $F^{+/-}(0)$ are the carrier fluxes. In the case of a 2D system with a parabolic spectrum, $F^{+}(0)$ can be expressed as follows:

$$F^{+}(0) = \int_0^\infty D_{2D}(E) f(E) v_{\text{inj}}\, dE, \tag{2}$$

where $D_{2D}(E) = \frac{m^*}{\pi\hbar^2}\Theta(E - E_C)$ is the 2D density of states, expressed using the Heaviside step function, $f(E)$ is the Fermi distribution function, and v_{inj} is the carrier injection velocity. The integral may be evaluated as

$$F^{+}(0) = \frac{m^* v_{\text{inj}}}{\pi\hbar^2} \int_0^\infty \frac{\Theta(E - E_C)\, dE}{1 + \exp\left(\frac{E - E_F}{k_B T}\right)} = \frac{m^* v_{\text{inj}}}{\pi\hbar^2} \varsigma_0(E_F), \tag{3}$$

where $E_F = qV_{\text{CH}}$, V_{CH} is the voltage drop across the quantum capacitance. Using the same logic, we write down the relation for the flux moving in the backward direction from the drain:

$$F^{-}(L) = F^{+}(0) \frac{\varsigma_0\left(E_F - qV_{\text{DS}}\right)}{\varsigma_0(E_F)}. \tag{4}$$

For simplicity, we assume that the reflection probability of carriers is constant over the energy range of interest. Also, we assume that typical $V_{\text{DS}} < \frac{k_B T}{q}$, such that scattering is the same for carriers going from source to drain and vice versa. Hence, we have the following:

$$F^{-}(0) = rF^{+}(0) + (1 - r)F^{-}(L). \tag{5}$$

The final relation for current:

$$\begin{aligned} I_{\text{DS}} &= 2Wq\left[F^{+}(0) - F^{-}(0)\right] \\ &= 2Wq\left[F^{+}(0) - rF^{+}(0) - (1 - r)F^{+}(0)\frac{\varsigma_0\left(E_F - qV_{\text{DS}}\right)}{\varsigma_0(E_F)}\right] \\ &= 2WqF^{+}(0)\left[1 - r - (1 - r)\frac{\varsigma_0\left(E_F - qV_{\text{DS}}\right)}{\varsigma_0(E_F)}\right] \\ &= 2Wq\frac{m^* v_{\text{inj}}}{\pi\hbar^2}\varsigma_0(E_F)\left[1 - r - (1 - r)\frac{\varsigma_0\left(E_F - qV_{\text{DS}}\right)}{\varsigma_0(E_F)}\right]. \end{aligned} \tag{6}$$

V_{CH} is given by $\frac{C_{\text{OX}}}{C_{\text{OX}} + C_{\text{D}}}(V_{\text{BG}} - V_{\text{T}})$, where C_{OX} is the capacitance per unit area of the oxide ($C_{\text{OX}} = \varepsilon_{\text{OX}}/t$, where t is the thickness of the oxide), C_{D} is the quantum capacitance, V_{BG} is the applied back-gate voltage, and V_{T} is introduced to consider the work function difference between the gate material and MoS_2, and for the charges at the MoS_2/oxide interface.

4.1.2 Fitting Parameters

Due to source/drain contact resistance we only observe the effective drain bias $V_{\text{DS}} = V_{\text{app DS}} - I_{\text{DS}}(R_{\text{S}} + R_{\text{D}})$, where $V_{\text{app DS}}$ represents the applied drain bias, and R_{S} and R_{D} denote the resistances at the source and drain, respectively. As a straightforward expression of I_{DS} requires iterative solutions of the drain-voltage and drain-current equations, we will model $V_{\text{app DS}}$ as $V_{\text{DS}} = (1 - \beta)V_{\text{app DS}}$. Here, β is a variable fitting parameter, influenced by the source/drain contact resistances and drain biases. The backscattering coefficient r in a low-field limit can be described as $r = L/(L + \lambda)$, where L is the channel length and λ is a low-field momentum relaxation length, treated as a fitting parameter. We consider multiplying the current amplitude by a scaling factor A to account for the real value of v_{inj} as a portion of v_T. Also instead of $\frac{C_{\text{OX}}}{C_{\text{OX}} + C_{\text{D}}}$, we use C_{fit}. The dimensionless parameter C_{fit} represents the conversion factor between the real voltage applied to the gate and the effective voltage in the channel. Therefore, the final list of fitting parameters is $[A, V_T, r, \beta, C_{\text{fit}}]$.

4.1.3 Fitting

First we consider $I_{\text{DS}}(V_{\text{BG}})$:

Table 2 shows the values obtained after the fitting procedure. As can be seen, there is a tiny discrepancy in the values. For simplicity, let's consider the mean values of each parameter. Now, we

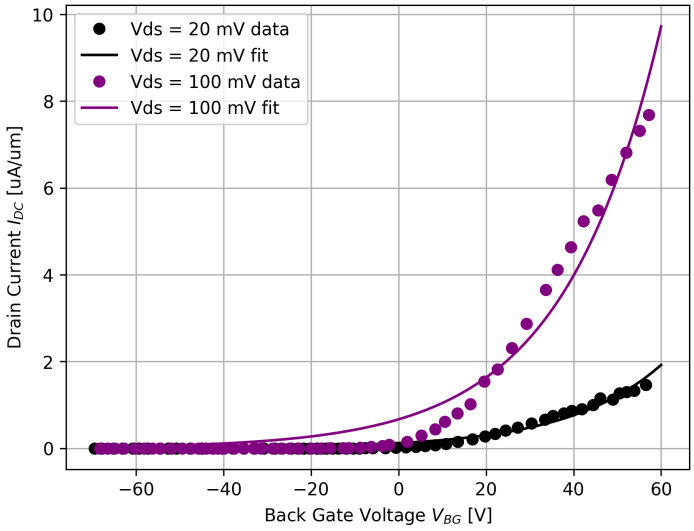

Figure 4: Fitting drain current dependency on back gate voltage for an 8nm channel.

V_{DS}	A	$V_T[\mathbf{V}]$	r	β	C_{fit}
20mV	0.77	11.248	0.80	0.998	0.001197
100mV	0.78	11.245	0.84	0.999	0.001154

Table 2: Values of the fitting parameters for the model.

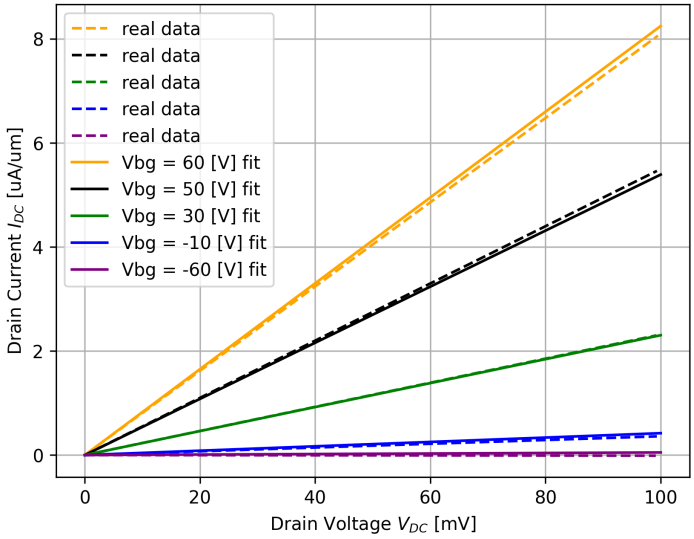

Figure 5: Fitting drain current dependency on drain voltage for an 8 [nm] channel.

can evaluate how well our fitting corresponds to the drain current dependence on drain voltage (Figure 3b in [1]).

Figure 5 illustrates the dependency of the source-drain current on the applied drain voltages. This dependency was fitted using the parameters obtained in the previous step, as summarized in Table 2. The resulting fit demonstrates excellent agreement with the published data.

4.1.4 Analysis

- $2R_c$: To compare the contact resistance calculated from fitting parameters with the experimentally obtained values, we use:

$$\beta = \frac{I_{\text{DS}}}{V_{\text{app DS}}}(R_{\text{S}} + R_{\text{D}}) = \frac{I_{\text{DS}}}{V_{\text{app DS}}} 2R_{\text{c}} \Rightarrow 2R_{\text{c}} = \beta \frac{V_{\text{app DS}}}{I_{\text{DS}}}$$

The results for $2R_c$ are presented in Figure 6.

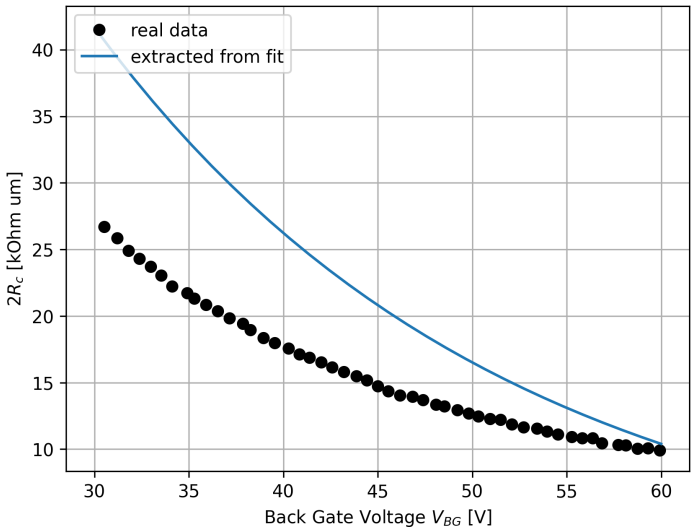

Figure 6: $2R_c$ dependence on V_{BG}. The real data is taken from Figure 4c [1].

In this analysis, one can observe a good estimation of contact resistance at 60 V, with an increasing error discrepancy as the voltage decreases. This can be attributed to the fact that the initial fitting was based on only two curves, representing the I_{DS} dependence on V_{BG} at drain voltages of 20 mV and 100 mV. The mean values of the fitting parameters from these curves were used to model the current. To address these discrepancies, a more refined model for gate-controlled population in the channel should be developed, or alternatively, more fitting parameter values should be extracted from a greater number of $I_{\text{DS}}(V_{\text{BG}})$ curves using the current model.

- μ: By fitting the backscattering coefficient r, we can estimate μ:

$$\mu = \frac{v_{\text{T}} q \lambda}{2k_B T} = \frac{v_{\text{T}} q L}{2k_B T} \frac{(1-r)}{r}$$

For $L = 8$ nm, the resulting $\mu \approx 28\,\text{cm}^2\text{V}^{-1}\text{s}^{-1}$, which is in excellent agreement with $\mu \approx 27\,\text{cm}^2\text{V}^{-1}\text{s}^{-1}$ reported in the publication.

- C_{fit}: The oxide capacitance C_{OX} can be calculated using the fabrication details provided in [1]. It is given by $C_{\text{OX}} = \frac{\varepsilon_{\text{OX}}}{t_{\text{OX}}} = 1.12 \times 10^{-4}$ [F/m^2]. For $C_{\text{fit}} = 11.97 \times 10^{-4}$ [F/m^2], the depletion capacitance C_{D} is determined to be 0.0935 [F/m^2]. This result indicates a predominant influence of the depletion capacitance, which is typical for a transistor in the ON state.

4.1.5 Discussion

Our model demonstrated adequate proficiency in fitting the experimental data. Employing parameters derived from the $I_{\text{DS}}(V_{\text{BG}})$ curve fitting (as shown in Figure 4), we successfully generated $I_{\text{DS}}(V_{\text{DS}})$ curves (refer to Figure 5) that closely matched the experimental observations. Furthermore, the extracted values of $2R_{\text{C}}$ (at $V_{\text{BG}} = 60$ V) and μ are in strong agreement with those reported in the referenced publication. However, it is important to acknowledge certain limitations. As evidenced in Figure 4, the initial fitting does exhibit some discrepancies. Moreover, the increasing discrepancy

in $2R_C(V_{BG})$ (illustrated in Figure 6) and the unusually high value of C_D highlight areas where our model assumptions could be refined. A critical area for improvement is the function h, which models how the gate voltage V_{BG} translates into the channel voltage $V_{CH} = h(V_{BG})$. Our current linear model is inadequate to provide a consistent fit across the entire range of V_{DS} and V_{BG} values. To produce a better fitting model, a more self-consistent approach considering both the field and carrier concentrations in a channel may be considered.

4.2 Additional Models: Non-Degeneracy & the Low Field Regime

Here we discuss two simplified models for fitting the data in the forward bias region, or once a near-linear region is observed. These models, although less rigorous than the previous discussion, offer key insight into the physical properties of the device in the ON state.

4.2.1 Non-Degenerate Quasi Ballistic

Applying the calculations used in part 4.1 while making the non-degenerate approximation ($E_C - E_F \geq 3k_BT$) about the bandstructure, we arrive at an alternative model that may be used to approximate the device at hand:

$$I_{DS} = WC(V_{BG} - V_T)\frac{v_T}{1 + \frac{2l_{eff}}{\lambda}}\frac{1 - e^{\frac{-eV_{DS}}{k_BT}}}{\frac{1}{1+r} + \frac{1-r}{1+r}e^{\frac{-eV_{DS}}{k_BT}}}, \tag{7}$$

where $v_T \equiv \sqrt{\frac{2k_BT}{\pi m*}}$ is the thermal velocity, l_{eff} is the effective channel length, λ is the mean free path, r is the reflection coefficient under the same assumption that $r_S = r_D$ made in the previous model, and $C = \frac{C_{OX}}{C_{OX}+C_D}$ as before.

The fitting parameters of such a model are V_T, l_{eff}/λ, and C, where we have fixed r=0.8 from our analysis in the first model. Because we know the channel length to be small L = 8nm $\approx l_{eff}$, fitting l_{eff}/λ approximates λ. This tells us whether the device behaves more ballistic ($L/\lambda << 1$), or resistive ($L/\lambda >> 1$). Fitting the reflection coefficient speaks to the resistance, which in a semi-classical model is proportional to $l_{eff}/(1-r)\lambda$. Finally, the capacitance should be fitted to account for discrepancies in the gate voltage, as was mentioned in the previous section. There is a caveat for fitting the non-degenerate quasi-ballistic model to the data given in the publication. The nature of the exponential decay in V_{DS} causes I_{DS} to plateau if room temperature (T = 300K) is assumed since $V_{DS,Sat} \approx k_bT/q$, so accurately fitting to I_{DS} vs. V_{DS} data was found to be not applicable.

4.2.2 Low Field Regime

A less rigorous model for 'back-of-the-envelope' calculations may be a linear IV relation in the low-field regime. For a device with channel length L, width W, operating at $V_{BG} > 0$, $V_{DS} < k_BT/q$,

$$I_{DS,\text{Low Field}} \approx \frac{W}{L}\mu' C(V_{BG} - V_T)V_{DS}, \tag{8}$$

where $\mu' = (\frac{1}{\mu_B} + \frac{1}{\mu})^{-1}$ is the effective mobility – the analytical Ballistic mobility $\mu_B \equiv \frac{qL\nu_T}{2k_BT}$ and a correction term in parallel. Like the last models, the low-field approximation fits V_T, but unlike these models, it fits the prefactor μ' by changing the correction term μ, instead of the capacitance.

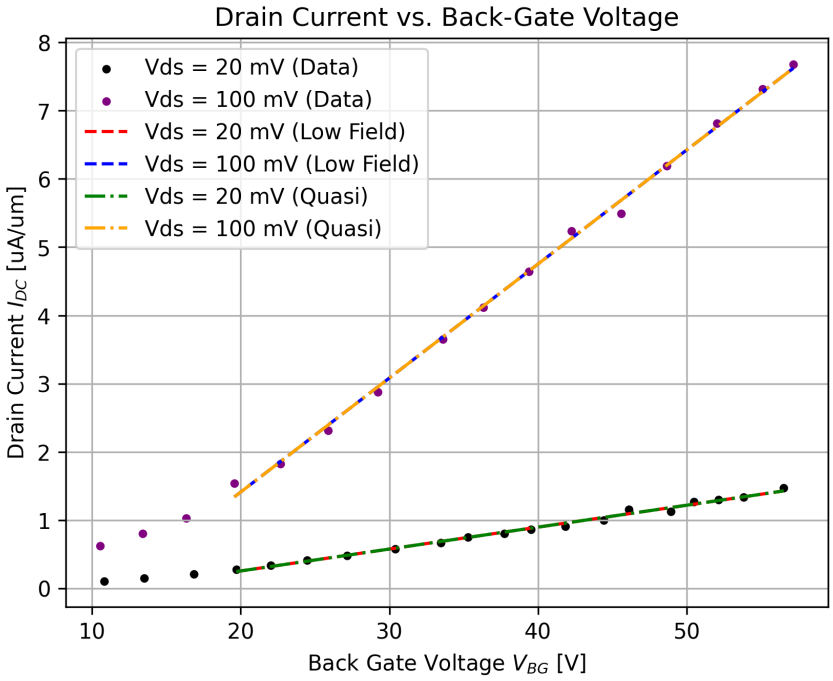

Figure 7: Fitted Non-Degenerate Quasi-Ballistic and Low Field models fit to I_{DS} vs. V_{BG} data.

4.2.3 Results

Fitting these models resulted in the parameters found in Tables 3 and 4. The fits are plotted in Fig. 7 and 8. Note that the reference voltage tends to agree with the primary model discussed earlier. Further, the fitted capacitance in the non-degenerate approximation is on the right order of magnitude. Interestingly, we have $l_{eff}/\lambda >> 1$ regardless of the drain voltage. This tells us that the FET is behaving similarly to a resistor. From our fits of the mobility correction, we find mobility higher than reported in the publication, $\mu' = 43.125$, as calculated by Matthiessen's rule.

V_{DS}	$V_T[\mathbf{V}]$	l_{eff}/λ	$C_{\text{fit}}[\text{F/m}^2]$
20mV	12.08	631.789	0.308×10^{-3}
100mV	11.564	995.607	2.527×10^{-3}

Table 3: Values of the fitting parameters for the Non-Degenerate Quasi-Ballistic model.

V_{DS}	$V_T[\mathbf{V}]$	$\mu[\text{cm}^2/\text{Vs}]$
20mV	12.08	41.579
100mV	11.564	43.290

Table 4: Values of the fitting parameters for the Low Field model.

4.2.4 Discussion

As we found with the explicit modeling done in Sec. 4.1, an exponential function does not capture the IV relationship of this device in the strong forward bias regime $V_{BG} \geq 20\text{V}$. Therefore, we seek linear approximations valid under the device's conditions. In this section, we observed two potential models that may lead to a better approximation of the device's behavior beyond the threshold voltage. We found that the linear IV relationship requires $l_{eff}/\lambda >> 1$ implying highly resistive behavior when V_{BG} is large and positive. This can equivalently be interpreted as a substantial correction to the ballistic mobility of charge carriers, as we found with the Low Field approximation.

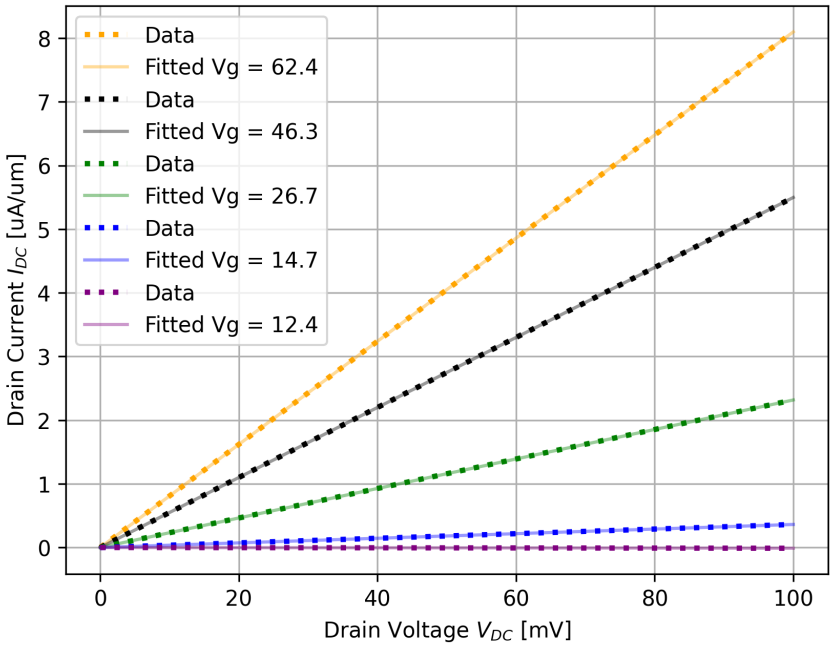

Figure 8: Low Field models fit to I_{DS} vs. V_{DS} data. We can observe how the model fails as $V_g \rightarrow < 0$. While the linear fit is successful in the positive regime, it does not take into account the IV behavior near the threshold voltage. As such, we see the model fit the incorrect gate voltage at low V_{BG}.

5 Conclusion

This report summarizes modeling and analysis done on a back-gated FET with a MoS_2 channel that uses graphene for metal contacts. Fabrication and characterization of the device are presented in [1] and represent a stone overturned in the search for new materials to incorporate in future electronics. By modeling the extracted data with several models ranging in complexity, we have found interesting traits of the device channel thought to be credited to the TMD. In particular, we found the device to behave in a resistive manner at $V_{BG} > V_T$, similar to short-channel Si devices. However, the physical contributions to the resistivity may come from various other sources such as imperfections during the fabrication process, and electron-electron interactions that are out of the scope of this report.

New device technologies require scalable fabrication techniques, and although 2D materials may scale down, devices composed of these materials cannot scale up. Currently, TMDs must be grown, often using Molecular Beam Epitaxy, while high-quality graphene must be manually exfoliated from graphite – a tedious extraction process that does not open doors to wide-scale production. As we have shown in our analysis, the device properties are not outstanding. We conclude that at this point such a device does not have commercial viability, but TMDs may be involved in future transistor technologies depending on the direction of research.

6 Resources

The code used for this analysis may be found on GitHub: https://github.com/eliaslehman/EE230.

Index	Basis Function
1	$d_{xz}^{(\mathrm{o})} = d_{xz}$
2	$d_{yz}^{(\mathrm{o})} = d_{yz}$
3	$p_z^{(\mathrm{o})} = \frac{1}{\sqrt{2}}\left(p_z^A + p_z^B\right)$
4	$p_x^{(\mathrm{o})} = \frac{1}{\sqrt{2}}\left(p_x^A - p_x^B\right)$
5	$p_y^{(\mathrm{o})} = \frac{1}{\sqrt{2}}\left(p_y^A - p_y^B\right)$
6	$d_{z^2}^{(\mathrm{e})} = d_{z^2}$
7	$d_{xy}^{(\mathrm{e})} = d_{xy}$
8	$d_{x^2-y^2}^{(\mathrm{e})} = d_{x^2-y^2}$
9	$p_z^{(\mathrm{e})} = \frac{1}{\sqrt{2}}\left(p_z^A - p_z^B\right)$
10	$p_x^{(\mathrm{e})} = \frac{1}{\sqrt{2}}\left(p_x^A + p_x^B\right)$
11	$p_y^{(\mathrm{e})} = \frac{1}{\sqrt{2}}\left(p_y^A + p_y^B\right)$

Table 5: New basis orbitals for tight-binding formalism

7 Appendix A

The tight-binding Hamiltonian is given by

$$\mathcal{H}(k) = \mathcal{H}^{(1)} + \mathcal{H}'^{(1)}$$

The diagonal terms of the tight-binding Hamiltonian take the form:

$$\mathcal{H}_{i,i}^{(1)}(\boldsymbol{k}) = \epsilon_i + 2t_{i,i}^{(1)} \cos \boldsymbol{k}\cdot\boldsymbol{\delta}_1 + 2t_{i,i}^{(2)} \left[\cos\left(\boldsymbol{k}\cdot\boldsymbol{\delta}_2\right) + \cos\left(\boldsymbol{k}\cdot\boldsymbol{\delta}_3\right)\right]$$

Due to the symmetry of the i and j orbitals: for $(i,j) = (3,5),(6,8),(9,11)$, the symmetry is $(+)$, giving

$$\mathcal{H}_{i,j}^{(1)}(\boldsymbol{k}) = 2t_{i,j}^{(1)} \cos \boldsymbol{k}\cdot\boldsymbol{\delta}_1 + t_{i,j}^{(2)}\left[e^{-i\boldsymbol{k}\cdot\boldsymbol{\delta}_2} + e^{-i\boldsymbol{k}\cdot\boldsymbol{\delta}_3}\right] + t_{i,j}^{(3)}\left[e^{i\boldsymbol{k}\cdot\boldsymbol{\delta}_2} + e^{i\boldsymbol{k}\cdot\boldsymbol{\delta}_3}\right]$$

For $(i,j) = (1,2),(3,4),(4,5),(6,7),(7,8),(9,10),(10,11)$, the symmetry is $(-)$, giving

$$\mathcal{H}_{i,j}^{(1)}(\boldsymbol{k}) = -2it_{i,j}^{(1)} \sin \boldsymbol{k}\cdot\boldsymbol{\delta}_1 + t_{i,j}^{(2)}\left[e^{-i\boldsymbol{k}\cdot\boldsymbol{\delta}_2} - e^{-i\boldsymbol{k}\cdot\boldsymbol{\delta}_3}\right] + t_{i,j}^{(3)}\left[-e^{i\boldsymbol{k}\cdot\boldsymbol{\delta}_2} + e^{i\boldsymbol{k}\cdot\boldsymbol{\delta}_3}\right]$$

For the pairs $(i,j) = (3,1),\ (5,1),(4,2),(10,6),(9,7),(11,7),(10,8)$, the symmetry is $(+)$, giving

$$\mathcal{H}_{i,j}^{(1)}(\boldsymbol{k}) = t_{i,j}^{(4)}\left[e^{i\boldsymbol{k}\cdot\boldsymbol{\delta}_4} - e^{i\boldsymbol{k}\cdot\boldsymbol{\delta}_6}\right]$$

For the pairs $(i,j) = (4,1),(3,2),(5,2),(9,6),(11,6),\ (10,7),(9,8),(11,8)$,

$$\mathcal{H}_{i,j}^{(1)}(\boldsymbol{k}) = t_{i,j}^{(4)}\left[e^{i\boldsymbol{k}\cdot\boldsymbol{\delta}_4} + e^{i\boldsymbol{k}\cdot\boldsymbol{\delta}_6}\right] + t_{i,j}^{(5)} e^{i\boldsymbol{k}\cdot\boldsymbol{\delta}_5}$$

And $\mathcal{H}_{i,j}^{(1)}(\boldsymbol{k}) = \mathcal{H}_{j,i}^{(1)}(\boldsymbol{k})^*$ and otherwise unassigned $\mathcal{H}_{i,j}^{(1)}(\boldsymbol{k})$ terms are zero. The correction matrix

$\mathcal{H}'^{(1)}_{i,i}$ from the second nearest hopping is given by

$$\begin{aligned}
\mathcal{H}'^{(1)}_{9,6}(\boldsymbol{k}) &= t^{(6)}_{9,6}\left(e^{i\boldsymbol{k}\cdot\boldsymbol{\delta}_7}+e^{i\boldsymbol{k}\cdot\boldsymbol{\delta}_8}+e^{i\boldsymbol{k}\cdot\boldsymbol{\delta}_9}\right)\\
\mathcal{H}'^{(1)}_{11,6}(\boldsymbol{k}) &= t^{(6)}_{11,6}\left(e^{i\boldsymbol{k}\cdot\boldsymbol{\delta}_7}-\frac{1}{2}e^{i\boldsymbol{k}\cdot\boldsymbol{\delta}_8}-\frac{1}{2}e^{i\boldsymbol{k}\cdot\boldsymbol{\delta}_9}\right)\\
\mathcal{H}'^{(1)}_{10,6}(\boldsymbol{k}) &= \frac{\sqrt{3}}{2}t^{(6)}_{11,6}\left(-e^{i\boldsymbol{k}\cdot\boldsymbol{\delta}_8}+e^{i\boldsymbol{k}\cdot\boldsymbol{\delta}_9}\right)\\
\mathcal{H}'^{(1)}_{9,8}(\boldsymbol{k}) &= t^{(6)}_{9,8}\left(e^{i\boldsymbol{k}\cdot\boldsymbol{\delta}_7}-\frac{1}{2}e^{i\boldsymbol{k}\cdot\boldsymbol{\delta}_8}-\frac{1}{2}e^{i\boldsymbol{k}\cdot\boldsymbol{\delta}_9}\right)\\
\mathcal{H}'^{(1)}_{9,7}(\boldsymbol{k}) &= \frac{\sqrt{3}}{2}t^{(6)}_{9,8}\left(-e^{i\boldsymbol{k}\cdot\boldsymbol{\delta}_8}+e^{i\boldsymbol{k}\cdot\boldsymbol{\delta}_9}\right)\\
\mathcal{H}'^{(1)}_{10,7}(\boldsymbol{k}) &= \frac{3}{4}t^{(6)}_{11,8}\left(e^{i\boldsymbol{k}\cdot\boldsymbol{\delta}_8}+e^{i\boldsymbol{k}\cdot\boldsymbol{\delta}_9}\right)\\
\mathcal{H}'^{(1)}_{11,7}(\boldsymbol{k}) &= \mathcal{H}'^{(1)}_{10,8}(\boldsymbol{k}) = \frac{\sqrt{3}}{4}t^{(6)}_{11,8}\left(e^{i\boldsymbol{k}\cdot\boldsymbol{\delta}_8}-e^{i\boldsymbol{k}\cdot\boldsymbol{\delta}_9}\right)\\
\mathcal{H}'^{(1)}_{11,8}(\boldsymbol{k}) &= t^{(6)}_{11,8}\left(e^{i\boldsymbol{k}\cdot\boldsymbol{\delta}_7}+\frac{1}{4}e^{i\boldsymbol{k}\cdot\boldsymbol{\delta}_8}+\frac{1}{4}e^{i\boldsymbol{k}\cdot\boldsymbol{\delta}_9}\right)
\end{aligned}$$

The tight-binding parameters are given by

	Values(eV)		**Values(eV)**		**Values(eV)**		**Values(eV)**
$\epsilon_1=\epsilon_2$	1.0688	$t^{(1)}_{4,4}$	0.8651	$t^{(1)}_{9,11}$	0.0075	$t^{(5)}_{5,2}$	2.1584
ϵ_3	−0.7755	$t^{(1)}_{5,5}$	−0.1872	$t^{(1)}_{1,2}$	−0.2562	$t^{(5)}_{9,6}$	−0.8836
$\epsilon_4=\epsilon_5$	−1.2902	$t^{(1)}_{6,6}$	−0.2979	$t^{(1)}_{3,4}$	−0.0995	$t^{(5)}_{11,6}$	−0.9402
ϵ_6	−0.1380	$t^{(1)}_{7,7}$	0.2747	$t^{(1)}_{4,5}$	−0.0705	$t^{(5)}_{10,7}$	1.4114
$\epsilon_7=\epsilon_8$	0.0874	$t^{(1)}_{8,8}$	−0.5581	$t^{(1)}_{6,7}$	−0.1145	$t^{(5)}_{9,8}$	−0.9535
ϵ_9	−2.8949	$t^{(1)}_{9,9}$	−0.1916	$t^{(1)}_{7,8}$	−0.2487	$t^{(5)}_{11,8}$	0.6517
$\epsilon_{10}=\epsilon_{11}$	−1.9065	$t^{(1)}_{10,10}$	0.9122	$t^{(1)}_{9,10}$	0.1063	$t^{(6)}_{9,6}$	−0.0686
$t^{(1)}_{1,1}$	−0.2069	$t^{(1)}_{11,11}$	0.0059	$t^{(1)}_{10,11}$	−0.0385	$t^{(6)}_{11,6}$	−0.1498
$t^{(1)}_{2,2}$	0.0323	$t^{(1)}_{3,5}$	−0.0679	$t^{(5)}_{4,1}$	−0.7883	$t^{(6)}_{9,8}$	−0.2205
$t^{(1)}_{3,3}$	−0.1739	$t^{(1)}_{6,8}$	0.4096	$t^{(5)}_{3,2}$	−1.3790	$t^{(6)}_{11,8}$	−0.2451

For the sets of indexes: $(\alpha=1,\beta=2),(\alpha=4,\beta=5,\gamma=3)$, $(\alpha=7,\beta=8,\gamma=6),(\alpha=10,\beta=11,\gamma=9)$ with the first superscript index corresponding to $(+)$ and the second to $(-)$, we have the following relations:

$$\begin{aligned}
\epsilon_\alpha &= \epsilon_\beta\\
t^{(2)}_{\alpha,\alpha} &= \frac{1}{4}t^{(1)}_{\alpha,\alpha}+\frac{3}{4}t^{(1)}_{\beta,\beta}\\
t^{(2)}_{\beta,\beta} &= \frac{3}{4}t^{(1)}_{\alpha,\alpha}+\frac{1}{4}t^{(1)}_{\beta,\beta}\\
t^{(2)}_{\gamma,\gamma} &= t^{(1)}_{\gamma,\gamma}\\
t^{(2,3)}_{\gamma,\beta} &= \pm\frac{\sqrt{3}}{2}t^{(1)}_{\gamma,\alpha}-\frac{1}{2}t^{(1)}_{\gamma,\beta}\\
t^{(2,3)}_{\alpha,\beta} &= \pm\frac{\sqrt{3}}{4}\left(t^{(1)}_{\alpha,\alpha}-t^{(1)}_{\beta,\beta}\right)-t^{(1)}_{\alpha,\beta}\\
t^{(2,3)}_{\gamma,\alpha} &= \frac{1}{2}t^{(1)}_{\gamma,\alpha}\pm\frac{\sqrt{3}}{2}t^{(1)}_{\gamma,\beta}
\end{aligned}$$

while for $(\alpha = 1, \beta = 2, \alpha' = 4, \beta' = 5, \gamma' = 3), (\alpha = 7, \beta = 8, \alpha' = 10, \beta' = 11, \gamma' = 9)$, we have:

$$
\begin{aligned}
t^{(4)}_{\alpha',\alpha} &= \frac{1}{4} t^{(5)}_{\alpha',\alpha} + \frac{3}{4} t^{(5)}_{\beta',\beta} \\
t^{(4)}_{\beta',\beta} &= \frac{3}{4} t^{(5)}_{\alpha',\alpha} + \frac{1}{4} t^{(5)}_{\beta',\beta} \\
t^{(4)}_{\beta',\alpha} = t^{(4)}_{\alpha',\beta} &= -\frac{\sqrt{3}}{4} t^{(5)}_{\alpha',\alpha} + \frac{\sqrt{3}}{4} t^{(5)}_{\beta',\beta} \\
t^{(4)}_{\gamma',\alpha} &= -\frac{\sqrt{3}}{2} t^{(5)}_{\gamma',\beta} \\
t^{(4)}_{\gamma',\beta} &= -\frac{1}{2} t^{(5)}_{\gamma',\beta} \\
t^{(4)}_{9,6} = t^{(5)}_{9,6}, t^{(4)}_{10,6} &= \frac{-\sqrt{3}}{2} t^{(5)}_{11,6}, t^{(4)}_{11,6} = \frac{-1}{2} t^{(5)}_{11,6}
\end{aligned}
$$

References

[1] Li Xie, Mengzhou Liao, Shuopei Wang, Hua Yu, Luojun Du, Jian Tang, Jing Zhao, Jing Zhang, Peng Chen, Xiaobo Lu, Guole Wang, Guibai Xie, Rong Yang, Dongxia Shi, and Guangyu Zhang. Graphene-contacted ultrashort channel monolayer mos2 transistors. *Advanced materials (Weinheim)*, 29(37), 2017.

[2] Shiang Fang, Rodrick Kuate Defo, Sharmila N. Shirodkar, Simon Lieu, Georgios A. Tritsaris, and Efthimios Kaxiras. Ab initio tight-binding hamiltonian for transition metal dichalcogenides. *Physical review. B*, 92(20), 2015.

[3] Anubhav Jain, Shyue Ping Ong, Geoffroy Hautier, Wei Chen, William Davidson Richards, Stephen Dacek, Shreyas Cholia, Dan Gunter, David Skinner, Gerbrand Ceder, and Kristin A. Persson. Commentary: The materials project: A materials genome approach to accelerating materials innovation. *APL Materials*, 1(1):011002–011002–11, 2013.

[4] Eugene S. Kadantsev and Pawel Hawrylak. Electronic structure of a single mos2 monolayer. *Solid state communications*, 152(10):909–913, 2012.

[5] Guangxi Hu, Shuyan Hu, Ran Liu, Lingli Wang, Xing Zhou, and Ting-Ao Tang. Quasi-ballistic transport model for graphene field-effect transistor. *IEEE transactions on electron devices*, 60(7):2410–2414, 2013.